Towards Elastic Bone Characterization in Transcranial Ultrasound

Patrick Marty[a], Trevor Mitcham[b], Rehman Ali[b], Christian Boehm[a], Neb Duric[b], and Andreas Fichtner[a]

[a]ETH Zurich, Institute of Geophysics, Switzerland
[b]University of Rochester Medical Center, United States of America

ABSTRACT

Constructing a physics-augmented digital twin of the skull is imperative for a wide range of transcranial ultrasound applications including ultrasound computed tomography and focused ultrasound therapy. The high impedance contrast as well as the acoustic-elastic coupling observed between soft tissue and bone increase the complexity of the ultrasound wavefield considerably, thus emphasizing the need for waveform-based inversion approaches. This work applies reverse time migration in conjunction with the spectral-element method to an *in vitro* human skull to obtain a starting model, which can be used for full-waveform inversion and adjoint-based shape optimization. Two distinct brain phantoms are considered where the cranial cavity of the *in vitro* human skull was filled with (1) homogeneous water and (2) gelatin with two cylindrical inclusions. A 2D slice through the posterior of the skull was collected using a ring-like aperture consisting of 1024 ultrasound transducers with a bandwidth of approximately 1 MHz to 3 MHz. Waveform-based reverse time migration was then used to resolve the inner and outer contours of the skull from which a conforming hexahedral finite-element mesh was constructed. The synthetically generated measurements which are obtained by solving the coupled acoustic-viscoelastic wave equation are in good agreement with the observed laboratory measurements. It is demonstrated that using this revised wave speed model for recomputing the reverse time migration reconstructions allows for improved localization of the gelatin inclusions within the cranial cavity.

Keywords: Ultrasound Computed Tomography, Transcranial Ultrasound, Spectral-Element Method, Reverse Time Migration, Full-Waveform Inversion, Shape Optimization

1. INTRODUCTION

Transcranial ultrasound computed tomography (USCT) is an emerging imaging modality which relies on transmitting ultrasound waves through the skull in order to recover reconstructions of the interior brain tissue.[1–4] This area of research has garnered significant interest in recent years given its ability to serve as an alternative to computed tomography (CT) or magnetic resonance imaging (MRI) for diagnosing and monitoring brain-related ailments.

While USCT may provide a radiation-free and potentially cost-effective alternative to existing imaging modalities, a number of significant technical challenges have thus far limited its adoption for transcranial applications. Two significant challenges within transcranial ultrasound are (1) the high impedance contrast at the bone interfaces causes the skull to act as a strong reflector[5,6] and (2) the occurrence of fluid-solid coupling between soft tissue and bone increases the complexity of the wavefield.[7–9]

The high impedance contrast at the soft tissue-bone interface severely limits the amount of signal which enters the skull given that a significant portion of the ultrasound waves are reflected at the skull boundaries. The significantly higher wave speeds within the skull also means that even slight thickness variations within the skull can lead to considerable distortions of the ultrasound wavefield. Thus, possessing an accurate model of the skull is imperative in order to correctly account for these deviations.[1,4]

Further author information: (Send correspondence to P.M.)
P.M.: E-mail: patrick.marty@erdw.ethz.ch

Medical Imaging 2024: Ultrasonic Imaging and Tomography, edited by Christian Boehm, Nick Bottenus, Proc. of SPIE Vol. 12932, 129320K · © 2024 SPIE · 1605-7422
doi: 10.1117/12.3006769

Most existing USCT approaches which are applied to imaging soft tissues assume that the tissues possess negligible shear moduli. This simplification is often referred to as the *acoustic approximation* and implies that the conversion of compressional (P-) to shear (S-) waves is minor within the tissues.[10,11] This is generally an excellent approximation within soft tissues, given that the P-wave speed is typically two to three orders of magnitude higher than the S-wave speed.[8,12] However, the significantly higher shear modulus in bones results in P- and S-wave speeds which are on the same order of magnitude. This leads to considerable conversions between P- and S-waves (and vice versa) at the soft tissue-bone interfaces; these effects become more pronounced for waves with steeper angles of incidence.[7]

In order to address these two complexities, this work explores strategies for recovering the shape of the skull using reverse time migration (RTM) in addition to modeling the acoustic-elastic coupling effects between soft tissue and bone using the spectral-element method (SEM). The use of these modeling approaches in the context of shape optimization and full-waveform inversion (FWI) are also discussed. The efficacy of these modeling procedures are demonstrated on two datasets collected for a tissue-mimicking phantom, which is contained within an *in vitro* human skull.

2. BACKGROUND AND METHODS

The proposed transcranial USCT approach involves using a combination of several well-established modeling and inversion approaches which are widely adopted in both seismology and medical ultrasound. In the following, a brief overview of the coupled acoustic-viscoelastic wave equation, spectral-element method, full-waveform inversion, reverse time migration, and shape optimization are provided.

2.1 Coupled Acoustic-Viscoelastic Wave Equation

The governing equations for describing the propagation of mechanical waves through various tissues are the acoustic and elastic wave equations for fluid and solid portions of the domain, respectively. For a full derivation of the wave equation, the reader is referred to Aki & Richards.[13]

Consider a domain Ω with spatial coordinates $\mathbf{x} \in \Omega \subset \mathbb{R}^2$ where Ω is composed of distinct acoustic and elastic regions such that $\Omega \coloneqq \Omega_\mathrm{a} \cup \Omega_\mathrm{e}$. The elastic wave equation is defined as

$$\rho(\mathbf{x})\partial_t^2\mathbf{u}(\mathbf{x},t) - \nabla\cdot\boldsymbol{\sigma}(\mathbf{x},t) = \mathbf{0} \tag{1}$$

given the time coordinate $t \in T \subset \mathbb{R}$, mass density ρ, displacement $\mathbf{u}$, and stress $\boldsymbol{\sigma}$. Given that the right-hand-side of equation (1) is zero, it is assumed that the elastic region Ω_e is source-free.

It is well known in the literature that the skull behaves as a highly attenuative medium.[5,14] This viscoelasticity is incorporated within the elastic wave equation through the addition of a time-dependent damping term, which acts to modify the stress.[15] Including attenuative effects, the stress-strain relation is modified such that the elastic tensor $\mathbf{C}$, which is implicitly dependent on the P- and S-wave speeds v_p and v_s, respectively, becomes time dependent. Thus, the stress-strain relation becomes

$$\boldsymbol{\sigma}(\mathbf{x},t) = \mathbf{C}(\mathbf{x},t) * \dot{\boldsymbol{\varepsilon}}(\mathbf{x},t) \tag{2}$$

where $\dot{\boldsymbol{\varepsilon}}$ is defined as the temporal derivative of the strain tensor and the temporal convolution is denoted by $*$.

The elastic wave equation outlined in equation (1) can be simplified for regions of the domain which possess negligible shear moduli. While not explicitly defined within equation (1), the shear modulus is encoded within the stress term. Under the assumption that the shear modulus $\mu(\mathbf{x}) \approx 0$, the elastic wave equation can be simplified to

$$\frac{1}{\rho(\mathbf{x})\,v_p^2(\mathbf{x})}\partial_t^2\varphi(\mathbf{x},t) - \nabla\cdot\left(\frac{1}{\rho(\mathbf{x})}\nabla\varphi(\mathbf{x},t)\right) = f(\mathbf{x},t) \tag{3}$$

for P-wave speed v_p, scalar potential φ, and source term f. The reason for which it is desirable to cast equation (1) into the form defined in equation (3) is that the acoustic wave equation is significantly less expensive to compute numerically when compared to its elastic counterpart. Note that the scalar potential φ can be interpreted as a pressure-like quantity where the second temporal derivative of the scalar potential $\partial_t^2\varphi$ is equivalent to the pressure.

These wave equations are coupled using interface conditions at the closed boundaries Γ_i which separate Ω_e and Ω_a.[16,17] The first interface condition given by

$$\boldsymbol{\sigma}(\mathbf{x},t)\cdot\hat{\boldsymbol{n}}(\mathbf{x}) = \rho(\mathbf{x})\,\partial_t^2\varphi(\mathbf{x},t)\,\hat{\boldsymbol{n}}(\mathbf{x}) \tag{4}$$

enforces the continuity of pressure in the normal direction to the interface. Similarly, the displacement is forced to be continuous in the normal direction to Γ_i using the second interface condition given by

$$\hat{\boldsymbol{n}}(\mathbf{x})\cdot\nabla\varphi(\mathbf{x},t) = \hat{\boldsymbol{n}}(\mathbf{x})\cdot\mathbf{u}(\mathbf{x},t). \tag{5}$$

These two conditions ensure that the waves which propagate through the acoustic regions of the domain are transmitted to the elastic regions (and vice versa).

Absorbing boundary conditions are applied on the outer-most boundary of the domain using a combination of the Sommerfeld radiation condition[18] and sponge layers.[19] The Sommerfeld condition absorbs most of the incoming ultrasound waves which have normal incidence to the outer boundaries. However, waves with steeper angles of incidence are only partially absorbed. The sponge layers introduce an attenuating region close to these outer boundaries, which leads to the absorption of remnant reflections that may not have been completely absorbed by the Sommerfeld condition.

2.2 Spectral-Element Method

A plethora of strategies exist for solving equations (1) and (3) numerically. One such approach, which is widely used in regional and global scale seismology, is the spectral-element method (SEM).[16,17,20] In addition to its use within seismological applications, the SEM has been shown to be an effective tool within medical ultrasound simulations.[9,21,22] The SEM is a specialized higher-order finite-element method which provides a number of attractive numerical properties to offer significant computational benefits over conventional finite-element approaches for solving the wave equation. The primary advantage of the SEM over other finite-element methods is that the mass matrix is diagonal by construction.[23] While conventional finite-element approaches typically require one to invert the mass matrix by solving a linear system, inverting this diagonal matrix in the SEM is trivial.

Another attractive property of the SEM is that the acoustic and elastic wave equations are solved independently for the different parts of the domain. The consequence of this is that the elastic wave equation must only be solved in Ω_e while the comparatively inexpensive acoustic wave equation can be solved for the rest of the domain Ω_a. This has significant implications from a computational standpoint for transcranial applications given that the proportion of elastic to acoustic elements within the domain is small. Thus, solving this coupled system for transcranial applications does not incur a significant penalty in terms of the overall computational cost when compared to solving the acoustic wave equation only.

While the SEM possesses many computational benefits, one of the primary challenges with applying the SEM to geometrically complex domains is that the spatial discretization must consist of a conforming hexahedral mesh.[24] The reason for this is that the diagonality of the mass matrix can only be guaranteed if hexahedral elements are used. Incorporating tetrahedral elements in the computational mesh tends to lead to a loss of the mass matrix's diagonality, which thus incurs a significant computational penalty. Furthermore, the inherently tensorized structure of hexahedral elements is lost when performing local gradient computations on tetrahedral elements, which leads to a further penalization in computational performance. Hybrid meshes comprised of a combination of hexahedral and tetrahedral elements could potentially be a strategy to overcome these meshing challenges, although this introduces considerable hurdles from an implementation standpoint to ensure appropriate load-balancing.

The automatic generation of fully-unstructured hexahedral meshes for geometries of arbitrary complexity remains an open problem in computational geometry.[25] While strategies exist in both 2D[26] and 3D[27] for constructing such meshes semi-automatically, applying these strategies to highly irregular geometries remains a challenge.[22]

The discrete formulations of equations (1) and (3) are not provided here in the interest of brevity. However, the reader is referred to works such as Komatitsch *et al.*[16] and Afanasiev *et al.*[17] for a comprehensive description of the discrete representation of these coupled wave equations.

2.3 Adjoint Method & Full-Waveform Inversion

A unique property of ultrasound imaging is that it is possible to directly invert for material properties such as density or wave speed; a proxy is not necessarily required. One inversion strategy which allows for these material properties to be recovered directly is full-waveform inversion (FWI).[28–30] This inversion algorithm is an iterative approach which involves minimizing the discrepancies between the observed ultrasound measurements and a set of synthetically computed ultrasound data (often colloquially referred to as *synthetics*). The objective of FWI is to iteratively update a set of model parameters that describes the material properties of the medium such that the observations are explained to within the measurement uncertainties.

One of the fundamental components of FWI is the process by which the synthetics are computed. This step involves solving the wave equation (sections 2.1 and 2.2) and, thus, typically dominates the overall computational cost of FWI. The material properties of ρ, v_p, and v_s represent the tissues through which the ultrasound waves propagate. Thus, given such a digital twin, physical phenomena such as reflection, transmission, and scattering can be modeled *in silico* in order to attempt to replicate the observed measurements.

Recovering a meaningful reconstruction of the tissues of the patient involves iteratively updating the space-dependent material properties of these tissues. This can be achieved by first defining a misfit function χ which quantifies the discrepancies between the observed measurements and a set of synthetically generated data. In order to reduce the discrepancies between these two sets of data, it is desirable to find the gradient of the misfit function with respect to the material property of interest $\mathbf{m}$. This gradient $\nabla_{\mathbf{m}}\chi$ effectively describes how the material properties should be modified in order to improve the fit between the observations and the synthetics.

A technique known as the *adjoint method* is typically employed to determine the gradient of the misfit function with respect to one or more model parameters. This approach first involves modeling the propagation of the forward wavefield through the domain of interest. Using the chosen misfit function, the so-called *adjoint sources* can be computed at each receiver position by comparing the synthetically generated data with the observed measurements. These adjoint sources are re-injected into the medium at the receiver locations in reverse time to allow for the back-propagation of the adjoint wavefield. This adjoint wavefield is then correlated with the previously computed forward wavefield in order to obtain the gradient of the misfit function.

For a comprehensive overview of FWI, the reader is referred to works such as Virieux & Operto[29] and Fichtner.[30] Examples of FWI being applied to transcranial USCT *in silico* are additionally explored in depth within works such as Guasch *et al.*[1] and Marty *et al.*[2]

2.4 Reverse Time Migration

Reverse time migration (RTM) is an imaging strategy which shares the same underlying physical principles as the adjoint method.[31,32] Specifically, a forward wavefield is correlated with a back-propagated adjoint wavefield to yield the RTM image. The RTM image itself can be interpreted as providing a map of the normalized impedance contrast throughout the domain. The primary differences between the adjoint method and conventional RTM are (1) the choice in adjoint source which is re-injected at the receiver positions in reverse time and (2) the fact that RTM is not generally performed in an iterative fashion.

In the adjoint method, the adjoint sources are computed based on the misfit function which quantifies the discrepancies between the observed measurements and the synthetically generated data. However, the adjoint sources in conventional RTM are chosen instead to be the entire observed signal at each receiver position. Thus, the RTM image $\zeta(\mathbf{x})$ can be computed by taking the directional derivative (denoted by $\nabla_\rho \ \cdot \delta\rho$) as

$$\nabla_\rho \zeta \cdot \delta\rho = \frac{1}{v_p} \int\limits_{\Omega} \int\limits_{T} \varphi^\dagger \cdot \nabla_\rho \mathbf{L}\left(\varphi\right) \delta\rho \ \mathrm{d}t \ \mathrm{d}^2\mathbf{x}, \tag{6}$$

where $\mathbf{L}$ is the forward wave operator describing equation (3) and $\varphi^\dagger$ is the adjoint wavefield which has been produced by re-injecting the observed measurements in reverse time. Note that the imaging condition used only considers the gradient with respect to the density ρ; an alternate mapping between fields is not used.

RTM is well suited for identifying the approximate positions of reflectors within the domain. While the presence of scatterers may be identifiable within the RTM reconstruction, the positional accuracy of these reflectors is directly dependent on how well the wave speed model for the domain is known. Incorrect wave speeds can result in the forward and adjoint wavefields being correlated at the incorrect position, thus resulting in the interface's position being shifted in space.

A conservative wave speed model with homogeneous properties consistent with the acoustic coupling fluid (water) between the transducers and the skull is considered in this work. This generally allows for the outer interfaces of the skull to be resolved effectively while the inner interfaces may be shifted due to the wave speed contrast between the water and the skull not being taken into account within this initial model.

2.5 Shape Optimization

As outlined in section 2.4, approaches such as RTM allow for the approximate interfaces of the skull to be identified.[2] However, the precise position of these interfaces is generally incorrect given that the precise wave speed model is not known *a priori*. A strategy which can be used to explicitly update the location of these interfaces is adjoint-based shape optimization.[33]

One can parameterize the shapes of the skull interfaces using a shape parameter γ. The process of shape optimization involves calculating the shape derivatives $\nabla_\gamma \chi$, which describe how the skull should be deformed in order to improve the fit between the observed measurements and the synthetics. These shape derivatives can be obtained by extracting the gradients of the misfit function $\nabla_{\mathbf{m}} \chi$ with respect to one of the material properties $[\rho, v_p, v_s] \in \mathbf{m}$ along the skull boundaries. Note that $\nabla_{\mathbf{m}} \chi$ can be computed numerically using the adjoint method, similar to the formulation defined in equation (6). An implicit assumption with this shape optimization approach is that the medium properties $\mathbf{m}$ are not updated at the same time as the shape parameter γ.

One of the benefits of inverting for the skull interfaces using shape optimization is that this serves as a convenient framework for preserving the distinct acoustic-elastic boundaries within the computational domains. Preserving this distinction between Ω_a and Ω_e is required such that the SEM solver knows which constituent equation to solve for a particular part of the medium. Preserving these interfaces ensures that the elemental boundaries between the acoustic and elastic regions within the hexahedral mesh continue to conform with the shape of the skull.

2.6 Data Acquisition

An *in vitro* human skull is the primary imaging target used throughout this study.[34] Two different material configurations are considered, where the cranial cavity is filled with (1) homogeneous water and (2) gelatin with two cylindrical inclusions. The gelatin inclusions within the second configuration have an approximate diameter of 11 mm and are intended to mimic blood clots within the brain tissue.

As can be seen in figure 1, a 1024-element ring array surrounds the posterior of the skull. This USCT measurement device consists of a Verasonics Vantage 256 system (Verasonics Inc., Kirkland WA), which is connected to the custom transducer array (TransducerWorks LLC, Centre Hall, PA; 3 MHz center frequency, 1 MHz to 3 MHz bandwidth). Each individual transducer element can act as both a source and a receiver, meaning that a total of 1024×1024 measurements are collected for each domain.

The primary software tools used for conducting the meshing and subsequent wave modeling are Coreform Cubit[36] and Salvus,[17] respectively. Given a set of closed non-intersecting contours which are identified from the RTM reconstruction, Coreform Cubit is used to generate hexahedral meshes of the domain where the element boundaries are set to conform with the delineated interfaces. These hexahedral meshes can then be used within Salvus for solving the coupled acoustic-viscoelastic wave equation in addition to solving the adjoint equations.

(a) Device configuration. (b) Cranial cavity filled with two gelatin inclusions.

Figure 1: The data acquisition configuration used for collecting the skull measurements. The ultrasound measurements consist of a 2D cross-sectional slice through the posterior of the skull. The example skull in this visualization is adapted from Iacono *et al.*[35]

3. RESULTS

The workflow considered can be categorized into the following components: (1) preprocessing of the raw data, (2) performing a source inversion to extract the individual source time functions for each transducer, (3) derive the RTM reconstructions for each domain, (4) extract the skull interfaces from the RTM images to construct an initial sound speed model, (5) use the revised initial model to improve the quality of the RTM reconstruction, and (6) use the RTM-derived mesh to compute shape derivatives and the gradients of the misfit functional with respect to the S-wave sound speed.

3.1 Preprocessing of the Raw Data

The ultrasound data can be visualized in the form of a *shot gather* where the collection of acquired ultrasound receivers are plotted for a single source position. Arrivals such as the direct wavefront through water or the reflections from the skull are apparent within such a representation. An example of such a shot gather representation where the raw observed data is compared with the preprocessed data can be seen in figure 2.

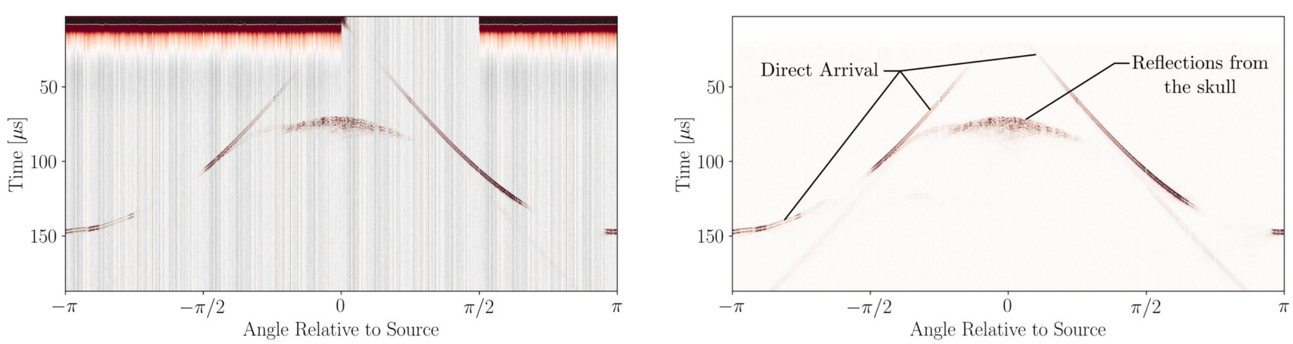

(a) Unfiltered data. (b) Filtered data.

Figure 2: A comparison between the unfiltered and the filtered measured data for the skull containing the gelatin inclusions. The filtering in the frequency-wavenumber domain as well as the use of a cosine taper in the time domain are intended to suppress the noise band prior to approximately 25 μs. A bandpass filter is further used to remove erroneous signal that is outside of the expected bandwidth of the transducers.

Three preprocessing stages are applied to the raw data in the form of (1) filtering in the frequency-wavenumber domain, (2) tapering in the time domain, and (3) bandpass filtering. This allows for the raw data in figure 2a to be filtered to obtain the data in figure 2b.

The filtering in the frequency-wavenumber domain involves applying a taper to suppress signals which possess very low wavenumbers. This assists in suppressing the noise which is apparent at the early onset times (before approximately 25 μs). The remaining signal within this noise band can then be filtered in the time domain using a cosine taper in order to mute the signal entirely for the early onset of the recordings.

In addition to the suppression of the noise band prior to approximately 25 μs, a bandpass filter is applied in order to remove extraneous signal which is outside of the expected transducer bandwidth. The manufacturer specifications suggest that the range of coherent ultrasound frequencies are within 1.0 MHz and 3.0 MHz. However, there is, indeed, some coherent signal which is evident beyond this limit. Given the importance of including low-frequency signal within potential FWI approaches, the observed data is filtered to approximately 0.2 MHz and 3.0 MHz.

3.2 Source Inversion

The source characteristics of each transducer are computed by performing a source inversion where the recorded ultrasound measurements are deconvolved from a set of simulated data.[37] A set of ultrasound measurements using the aforementioned device were collected for a configuration where no imaging target was present within the water bath; the ultrasound waves only propagated through the homogeneous water. This watershot dataset was deconvolved from synthetically generated measurements that were obtained by simulating the propagation of a Dirac delta function through homogeneous water. An example of one such inverted source wavelet can be seen in figure 3.

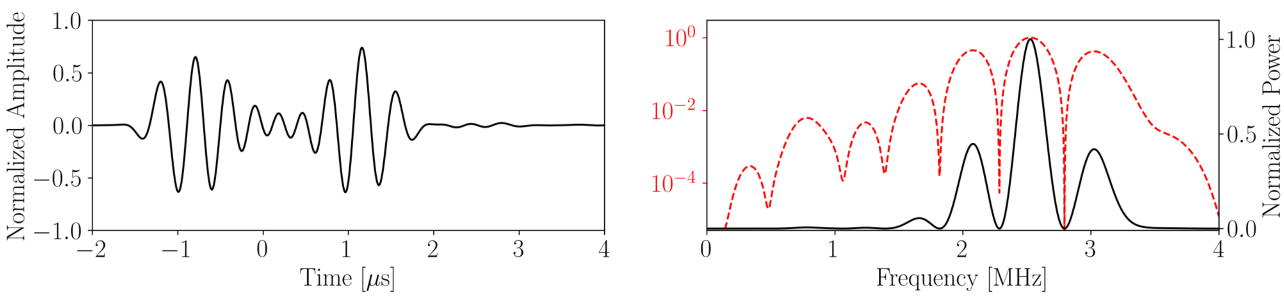

Figure 3: An example of one of the inverted source time functions with its time-domain representation (left) and corresponding power spectrum (right). Note that the power spectrum (right) is plotted both linearly (black) and logarithmically (red). While most of the signal is within the frequency range of approximately 1.5 MHz to 3.0 MHz, it can be seen within the logarithmic power spectrum that there is, indeed, some low-frequency content below 1.5 MHz.

While the source transducers are assumed to be identical across the entire device, slight deviations between the individual source time functions are to be expected due to subtle differences in coupling or manufacturing tolerances. However, as can be seen in figure 4, the inverted source wavelets are extremely similar across the various source transducers.

The inverted source time functions can be used to compute the expected waveforms through homogeneous water to offer a validation with the watershot collected with the measurement device. As can be seen in figure 5, there is excellent agreement between the watershot measurement and the synthetic data through the homogeneous water, thus giving confidence in the quality of the inverted source signatures.

3.3 Reverse Time Migration with a Homogeneous Wave Speed Model

Reverse time migration is applied to both of the datasets discussed in section 2.6. A homogeneous model consisting of water is considered as the background medium through which the forward and (time-reversed)

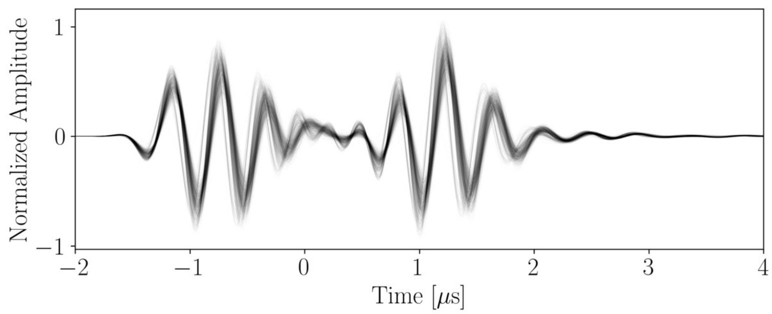

Figure 4: An overlay of all 1024 inverted source time functions. While the inverted wavelets are not completely identical, there is excellent agreement across the various source transducers.

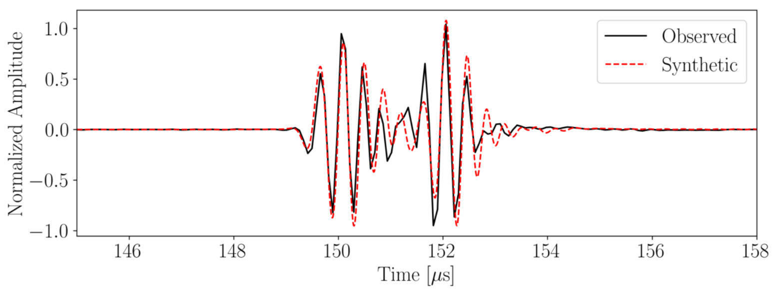

Figure 5: A comparison between the observed and synthetically generated watershot data. The synthetically generated data were modeled by solving the wave equation in a homogeneous medium using the inverted source time functions.

adjoint wavefields propagate. While this is certainly a conservative initial model, it is very well suited for delineating the outer skull interface given that the medium between the source and the skull also consists of homogeneous water. Thus, the position of the outer skull interface is expected to be fairly precise while the inner interface is likely to be shifted, given that the increased sound speed of the skull is not accounted for.

The RTM reconstructions are created using all 1024 source transducers with the sources being lowpass filtered to 1 MHz. A single forward and adjoint simulation is required for each source position, meaning that a total of 2048 wave simulations are performed to yield such an RTM image. The RTM reconstructions obtained for both of these domains can be seen in figure 6.

The inner and outer interfaces of the skull are resolved in both cases. It is worth noting that the inner interface is not simply an erroneous multiple reflection of the outer interface given that these two apparent reflectors are not parallel to one another. The inclusions within the case where a gelatin brain phantom was considered can also be identified, although the precise boundaries of the inclusions cannot be delineated. Similar to the expected mismatch in the inner skull boundary, this poor delineation of the interfaces of the gelatin inclusions can almost certainly be attributed to the inherently incorrect wave speed model considered.

3.4 Construct Revised Wave Speed Model

The inner and outer skull interfaces can be extracted from the RTM reconstructions depicted in figure 6. These interfaces serve as the basis for constructing an initial model which can be used for performing shape optimization and FWI. Using representative wave speed and density values from the literature,[8,38] the revised model depicted in figure 7 can be constructed. A summary of the properties assigned to the mesh in figure 7 are provided in table 1.

These interfaces are used to explicitly mesh the boundaries between the skull and the adjacent fluid media. Meshing these interfaces avoids potential staircasing artifacts which would otherwise pollute the wavefield at these distinct material boundaries. The model constructed in figure 7 is used to compute a set of synthetically

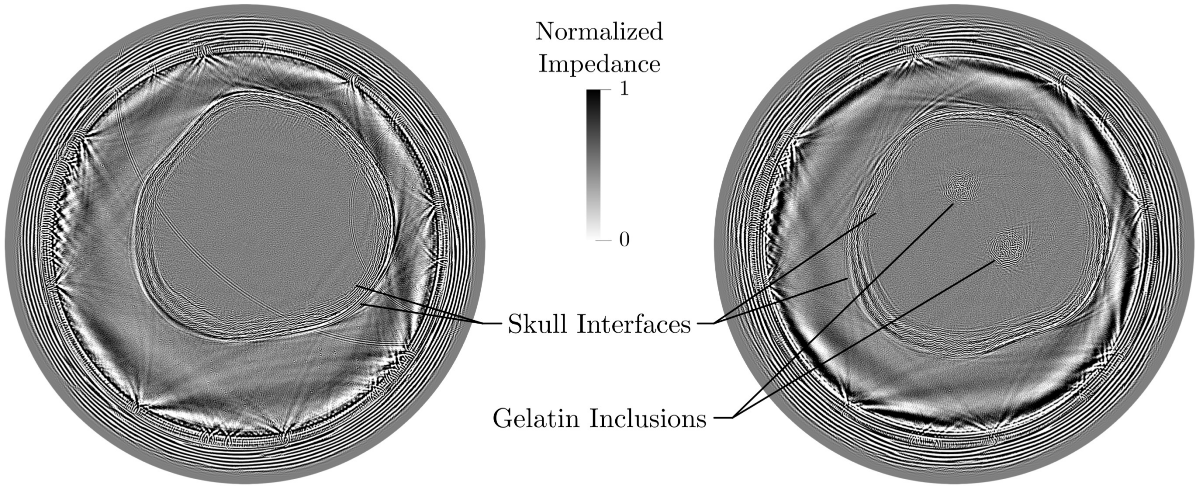

a) Water-filled skull. b) Gelatin-filled skull.

Figure 6: RTM images depicting the normalized impedance for the water- and gelatin-filled skulls. The inner and outer skull interfaces are apparent within both reconstructions. Furthermore, the gelatin inclusions within figure 6b are also evident within the reconstruction.

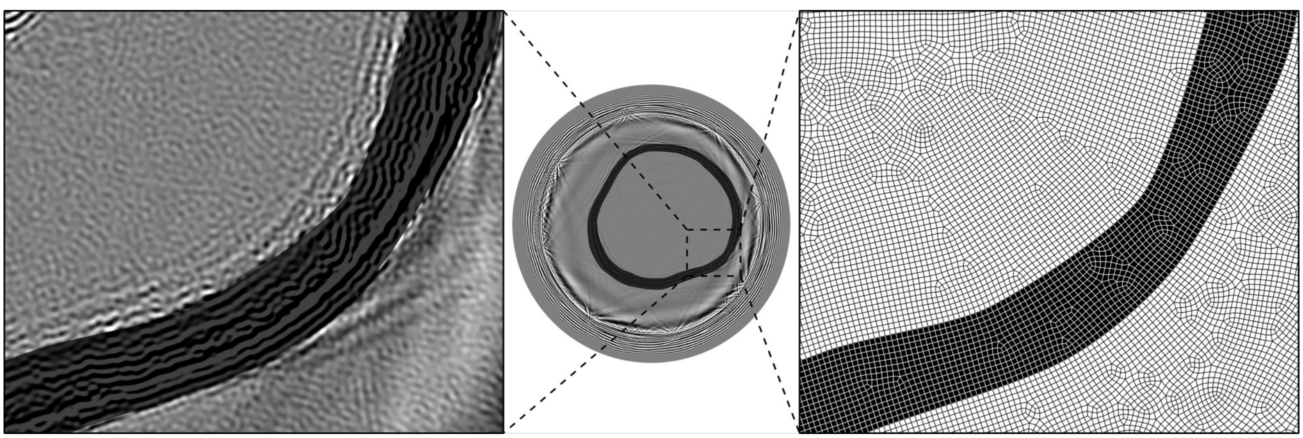

Figure 7: A close-up of the hexahedral mesh which has been constructed based on the RTM image. A transparent overlay of the extracted interfaces relative to the reflectors in the RTM image (left) and the hexahedral mesh itself (right) are shown.

Table 1: The reference material properties used for the skull in figure 7. The given material properties consist of the P-wave sound speed v_p, S-wave sound speed v_s, density ρ, P-wave attenuation α_p, and S-wave attenuation α_s. The P-wave sound speed in water was approximated using the watershot data from figure 5 while the material properties for the skull were chosen based on results from White *et al.*[8] and Pichardo *et al.*[38]

Material Property	v_p [m/s]	v_s [m/s]	ρ [kg/m^3]	α_p [Np/cm]	α_s [Np/cm]
Water	1456	0.0	997	N/A	N/A
Skull	2700	1550	1850	0.53	1.46

generated data to validate that the synthetic waveforms share the same overall structure as the observed data. A comparison of the observed measurements and the synthetically generated data computed using the mesh in figure 7 can be seen in figure 8.

Overall, the shot gathers shown in figures 8a and 8b share the same overall trend. In particular, there is

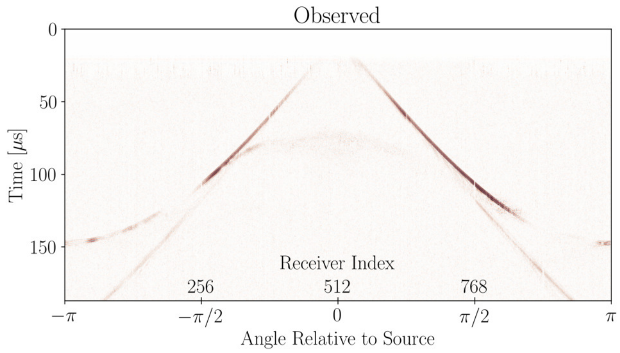

(a) Observed measurement.

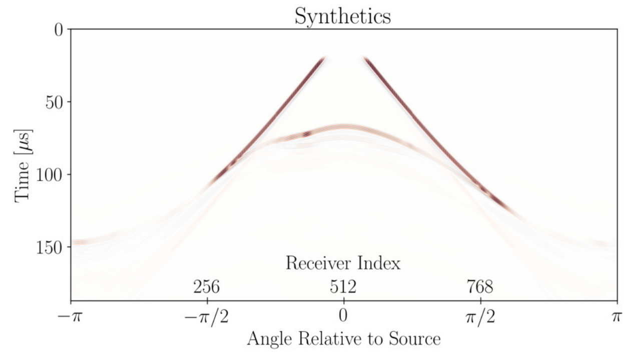

(b) Synthetics obtained by using the RTM-derived mesh.

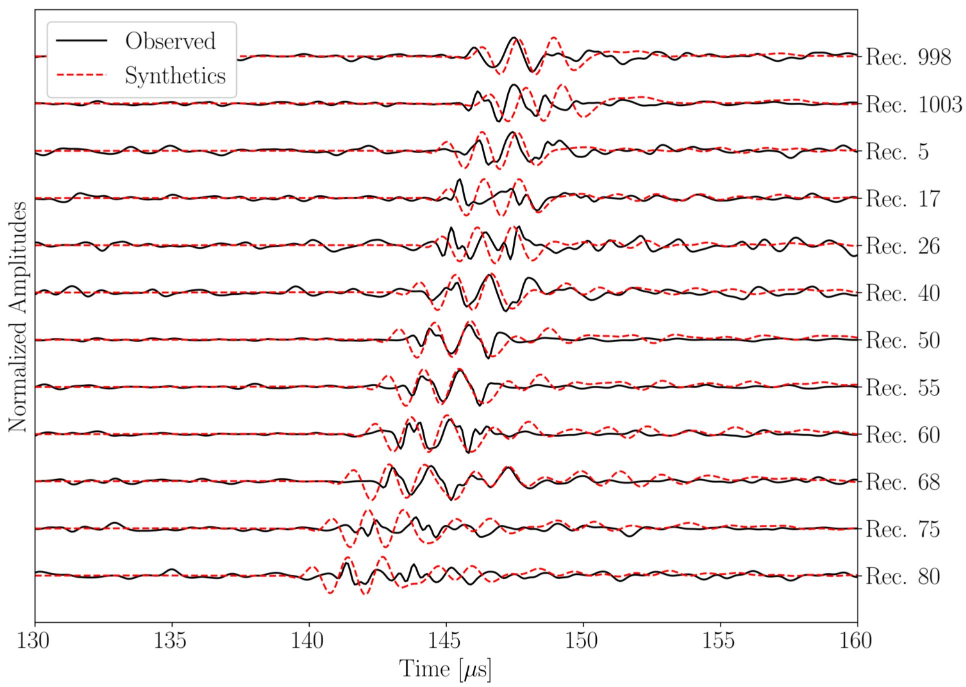

(c) Comparing individual ultrasound receiver traces. The receiver index is indicated to the right of each trace.

Figure 8: A comparison between the observed measurements and the synthetically generated forward data using the RTM-derived skull model depicted in figure 7. The shot gathers in figures 8a and 8b illustrate the overall agreement between the two datasets. The traces in figure 8c demonstrate the fit between individual signals from figures 8a and 8b. Given that the traces depicted in figure 8c correspond to the recorded signal on the opposite side of the skull, the primary arrivals within the plotted traces correspond to the waves which propagate through the skull and the interior brain tissue.

excellent agreement with the onset times of the reflected arrivals for receivers at angles θ_{r} between $\frac{-\pi}{2} < \theta_{\mathrm{r}} < \frac{\pi}{2}$. While these onset times are effectively matched between the two datasets, there is a distinct discrepancy in terms of the relative amplitude for the reflected arrival from the skull interface which is closest to the source. It is hypothesized that this discrepancy stems from the source characteristics used for computing the synthetically generated data. The synthetics were computed using an idealized point source instead of a finite-width distributed source, which thus results in the radiation pattern of the source transducer being neglected.

A prominent feature which is present within both the observed measurements and the synthetically generated data is the apparent gap in the transmitted arrivals around receiver angles of $\theta_\mathrm{r} \approx -\frac{\pi}{2}$ and $\theta_\mathrm{r} \approx \frac{3\pi}{4}$. This gap stems from the geometric effects of the skull, which results in the occurrence of a *shadow* in the wavefield close to the part of the wavefield which grazes the outer interface of the skull.

The comparison between the observed measurements and the synthetically generated data within figure 8c demonstrates that the proposed initial model constructed in figure 7 fits the transmitted arrivals quite effectively. It is worth noting that while there are certainly many secondary arrivals which are not captured by the model in figure 7, this model has not yet undergone any further optimization using FWI; this mesh would serve as the initial model for subsequently performing FWI or adjoint-based shape optimization.

3.5 Reverse Time Migration with the Revised Wave Speed Model

As noted in section 2.6, the diameter of each of the cylindrical inclusions is approximately 11 mm. However, the gelatin inclusions which are evident within figure 9a possess an apparent diameter of approximately 20 mm. This discrepancy can be attributed to the inherently incorrect sound speed model used to obtain the initial RTM reconstruction. In order to improve the size estimate of these inclusions, one can use the revised sound speed model defined in section 3.4; the resulting RTM reconstruction can be seen in figure 9b.

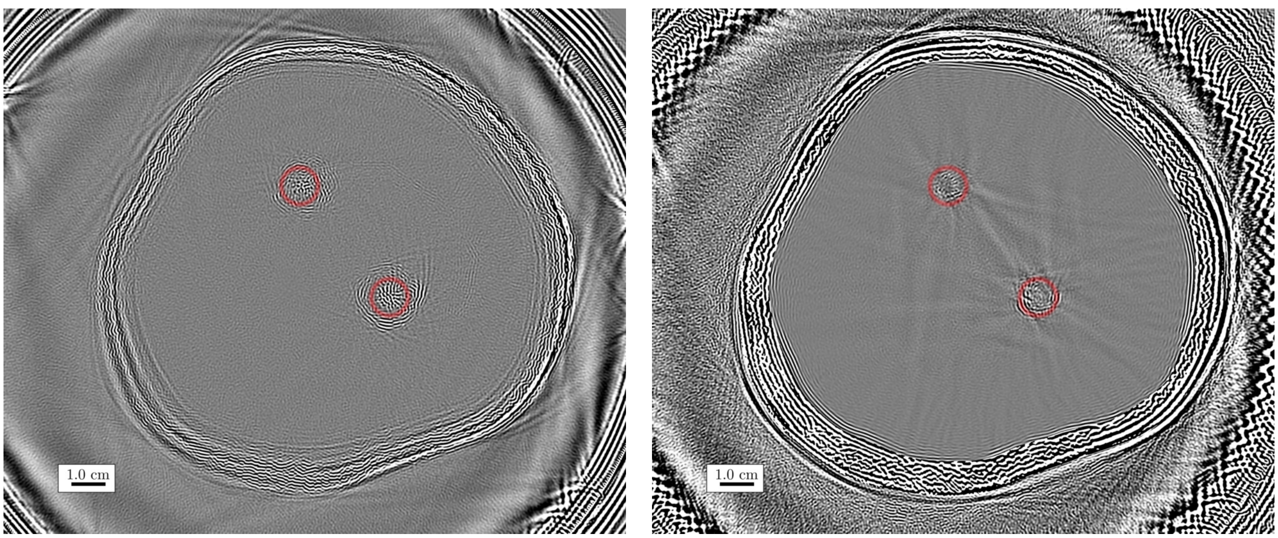

(a) Homogeneous wave speed model. (b) Revised wave speed model.

Figure 9: A comparison between the RTM reconstructions obtained using a wave speed model consisting of homogeneous water and the revised wave speed model defined in section 3.4. The transparent red overlays on both reconstructions illustrate the expected inclusion sizes of 11 mm. While the sizes of the inclusions in figure 9a are considerably overestimated, the reconstruction obtained in figure 9b using the revised wave speed model allow for the inclusions to be better constrained.

The use of a more accurate sound speed model causes the positions of the reflectors to be shifted in space. In comparing the sizes of the apparent inclusions in figure 9 with the idealized 11 mm inclusions overlain in red, it is evident in figure 9a that the sizes of the inclusions are significantly overestimated when a homogeneous sound speed model is used. However, the relative sizes of the inclusions is improved considerably in figure 9b when the revised sound speed model from figure 7 is used.

It is worth noting that some additional artifacts become apparent within the reconstruction within the revised sound speed model. In particular, additional streaking near the positions of the inclusions have been introduced. Improving the sound speed model further using an iterative inversion algorithm such as FWI would assist in suppressing these artifacts.

4. DISCUSSION AND OUTLOOK

One of the primary intentions of the sound speed model constructed in the section 3.4 is for it to serve as an initial model for performing FWI and shape optimization. The general approach of this inversion framework is to sequentially invert for (1) the approximate sound speed distribution within the skull using FWI and (2) the skull shape using shape optimization.

The adjoint equation is solved for the RTM-derived wave speed and density model outlined in section 3.4. In order to restrict model updates to be exclusively in the skull, a mask is applied to the gradient such as to exclude the fluid regions of the d omain. Solving the adjoint equation allows for the gradient $\nabla_{v_s}\chi$ to be obtained within the skull model. Note that it is preferable to consider the model parameter v_s instead of v_p in this case given the shorter wavelengths of the shear waves within the skull due to $v_s < v_p$. The shape derivatives $\nabla_\gamma\chi$ can be computed using $\nabla_{v_s}\chi$ in order to determine how the skull should be deformed such that the misfit χ is decreased. An example of the gradient $\nabla_{v_s}\chi$ and shape derivative $\nabla_\gamma\chi$ can be seen in figure 10.

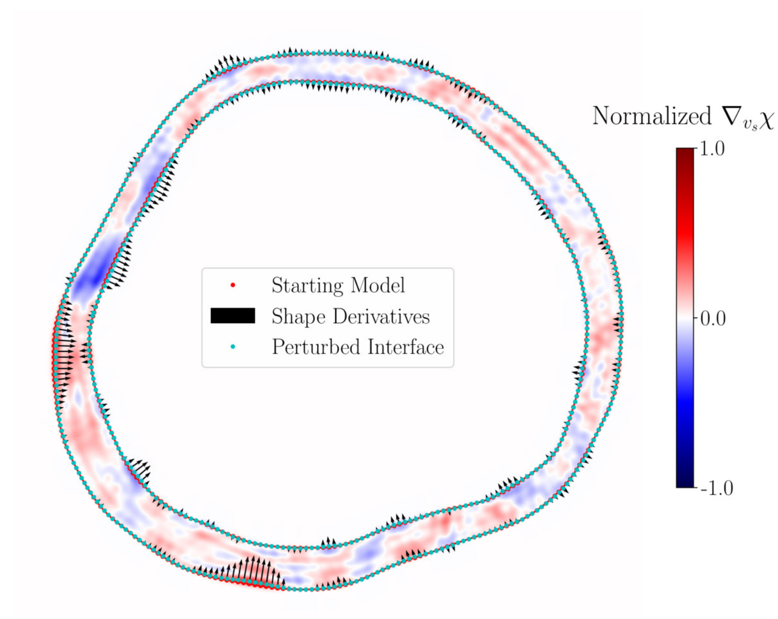

Figure 10: The shape derivatives $\nabla_\gamma\chi$ obtained using the gradients $\nabla_{v_s}\chi$ as a basis. The orientation of the shape derivatives indicate the direction along which the respective point on the interface is to be shifted. Similarly, the length of the shape derivatives indicate the relative magnitude of the perturbation which should be applied to the interface to lead to a decrease in the misfits χ.

The shape derivatives $\nabla_\gamma\chi$ in figure 10 illustrate locations where the skull should be locally deformed. It is worth noting that the gradients $\nabla_{v_s}\chi$ appear to delineate distinct structure within the skull for areas where the shape derivatives are small; examples include the regions at approximately 2 o'clock, 7-8 o'clock, and 11-12 o'clock. This implies that the gradients $\nabla_{v_s}\chi$ will lead to more meaningful model updates within the skull for the material properties once the overall shape of the skull has been optimized.

5. CONCLUSIONS

Full-waveform ultrasound modeling has been used to recover the cross-section of an *in vitro* human skull. This approach uses RTM to delineate the soft tissue-bone interfaces between the skull and the surrounding fluid media. These distinct fluid-solid boundaries are extracted and have been used to construct a hexahedral mesh where the element boundaries follow the soft tissue-bone interfaces. This computational domain is then used to solve the coupled acoustic-viscoelastic wave equation to obtain a set of synthetically generated data, which shows good agreement with the laboratory measurements. Recomputing the RTM reconstruction using the revised wave speed model shows improvement in the localization of the gelatin inclusions within the cranial cavity when compared to the RTM reconstruction obtained using a homogeneous water model. This revised wave speed model may be used in future studies as a basis for performing FWI and adjoint-based shape optimization in order to further refine the fit between the synthetically generated data and the observed measurements.

ACKNOWLEDGMENTS

This work was supported by the Swiss National Supercomputing Centre (CSCS) under project ID s1238.

REFERENCES

[1] Guasch, L., Calderón Agudo, O., Tang, M.-X., Nachev, P., and Warner, M., "Full-waveform inversion imaging of the human brain," *npj Digital Medicine* **3**, 28 (Feb. 2020).

[2] Marty, P., Boehm, C., and Fichtner, A., "Elastic Full-Waveform Inversion for Transcranial Ultrasound Computed Tomography using Optimal Transport," in [*2022 IEEE International Ultrasonics Symposium (IUS)*], (Oct. 2022). ISSN: 1948-5727.

[3] Orozco, R., Louboutin, M., Siahkoohi, A., Rizzuti, G., van Leeuwen, T., and Herrmann, F., "Amortized Normalizing Flows for Transcranial Ultrasound with Uncertainty Quantification," in [*Proceedings of Machine Learning Research*], **159**, 1–18 (2023).

[4] Robins, T. C., Cueto, C., Cudeiro, J., Bates, O., Agudo, O. C., Strong, G., Guasch, L., Warner, M., and Tang, M.-X., "Dual-Probe Transcranial Full-Waveform Inversion: A Brain Phantom Feasibility Study," *Ultrasound in Medicine & Biology* **49**, 2302–2315 (Oct. 2023).

[5] Fry, F. J. and Barger, J. E., "Acoustical properties of the human skull," *The Journal of the Acoustical Society of America* **63**, 1576–1590 (May 1978).

[6] Ylitalo, J., Koivukangas, J., and Oksman, J., "Ultrasonic reflection mode computed tomography through a skullbone," *IEEE Transactions on Biomedical Engineering* **37**, 1059–1066 (Nov. 1990).

[7] Clement, G., J White, P., and Hynynen, K., "Enhanced ultrasound transmission through the human skull using shear mode conversion," *The Journal of the Acoustical Society of America* **115**, 1356–64 (Apr. 2004).

[8] White, P. J., Clement, G. T., and Hynynen, K., "Longitudinal and shear mode ultrasound propagation in human skull bone," *Ultrasound in Medicine & Biology* **32**, 1085–1096 (July 2006).

[9] Marty, P., Boehm, C., and Fichtner, A., "Acoustoelastic full-waveform inversion for transcranial ultrasound computed tomography," in [*Medical Imaging 2021: Ultrasonic Imaging and Tomography*], **11602**, 1160211, International Society for Optics and Photonics (Feb. 2021).

[10] Wiskin, J. W., Borup, D. T., Iuanow, E., Klock, J., and Lenox, M. W., "3-D Nonlinear Acoustic Inverse Scattering: Algorithm and Quantitative Results," *IEEE Transactions on Ultrasonics, Ferroelectrics, and Frequency Control* **64**, 1161–1174 (Aug. 2017).

[11] Matthews, T. P., Wang, K., Li, C., Duric, N., and Anastasio, M. A., "Regularized Dual Averaging Image Reconstruction for Full-Wave Ultrasound Computed Tomography," *IEEE Transactions on Ultrasonics, Ferroelectrics, and Frequency Control* **64**, 811–825 (May 2017).

[12] Frizzell, L. A., Carstensen, E. L., and Dyro, J. F., "Shear properties of mammalian tissues at low megahertz frequencies," *The Journal of the Acoustical Society of America* **60**, 1409–1411 (Dec. 1976).

[13] Aki, K. and Richards, P., [*Quantitative Seismology*], University Science Books, Mill Valley, California, 2 ed. (2002).

[14] Pinton, G., Aubry, J.-F., Bossy, E., Muller, M., Pernot, M., and Tanter, M., "Attenuation, scattering, and absorption of ultrasound in the skull bone," *Medical Physics* **39**(1), 299–307 (2012).

[15] van Driel, M. and Nissen-Meyer, T., "Optimized viscoelastic wave propagation for weakly dissipative media," *Geophysical Journal International* **199**, 1078–1093 (Nov. 2014).

[16] Komatitsch, D., Barnes, C., and Tromp, J., "Wave propagation near a fluid-solid interface: A spectral-element approach," *Geophysics* **65**, 623–631 (Mar. 2000).

[17] Afanasiev, M., Boehm, C., van Driel, M., Krischer, L., Rietmann, M., May, D. A., Knepley, M. G., and Fichtner, A., "Modular and flexible spectral-element waveform modelling in two and three dimensions," *Geophysical Journal International* **216**, 1675–1692 (Mar. 2019).

[18] Sommerfeld, A., "Die Greensche Funktion der Schwingungsgleichung," in [*Jahresbericht der Deutschen Mathematiker-Vereinigung*], **21**, 309–353 (1912).

[19] Kosloff, R. and Kosloff, D., "Absorbing boundaries for wave propagation problems," *Journal of Computational Physics* **63**, 363–376 (Apr. 1986).

[20] Nissen-Meyer, T., Fournier, A., and Dahlen, F. A., "A 2-D spectral-element method for computing spherical-earth seismograms-II. Waves in solid-fluid media," *Geophysical Journal International* **174**, 873–888 (Sept. 2008).

[21] Bachmann, E. and Tromp, J., "Source encoding for viscoacoustic ultrasound computed tomography," *The Journal of the Acoustical Society of America* **147**, 3221–3235 (May 2020).

[22] Marty, P., Boehm, C., Paverd, C., Rominger, M., and Fichtner, A., "Full-waveform ultrasound modeling of soft tissue-bone interactions using conforming hexahedral meshes," in [*Medical Imaging 2022: Physics of Medical Imaging*], **12031**, 877–891, SPIE (Apr. 2022).

[23] Komatitsch, D. and Tromp, J., "Introduction to the spectral element method for three-dimensional seismic wave propagation," *Geophysical Journal International* **139**, 806–822 (Dec. 1999).

[24] Ferroni, A., Antonietti, P. F., Mazzieri, I., and Quarteroni, A., "Dispersion-dissipation analysis of 3-D continuous and discontinuous spectral element methods for the elastodynamics equation," *Geophysical Journal International* **211**, 1554–1574 (Dec. 2017).

[25] Pietroni, N., Campen, M., Sheffer, A., Cherchi, G., Bommes, D., Gao, X., Scateni, R., Ledoux, F., Remacle, J., and Livesu, M., "Hex-Mesh Generation and Processing: A Survey," *ACM Transactions on Graphics* **42**, 1–44 (Apr. 2023).

[26] Blacker, T. D. and Stephenson, M. B., "Paving: A new approach to automated quadrilateral mesh generation," *International Journal for Numerical Methods in Engineering* **32**(4), 811–847 (1991).

[27] Owen, S. J., Staten, M. L., and Sorensen, M. C., "Parallel hexahedral meshing from volume fractions," *Engineering with Computers* **30**, 301–313 (July 2014).

[28] Tarantola, A., "Inversion of seismic reflection data in the acoustic approximation," *Geophysics* **49**, 1259–1266 (Aug. 1984).

[29] Virieux, J. and Operto, S., "An overview of full-waveform inversion in exploration geophysics," *Geophysics* **74**, WCC1–WCC26 (Nov. 2009).

[30] Fichtner, A., [*Full Seismic Waveform Modelling and Inversion*], Advances in Geophysical and Environmental Mechanics and Mathematics, Springer-Verlag, Berlin Heidelberg (2011).

[31] Mulder, W. A. and Plessix, R., "A comparison between one-way and two-way wave-equation migration," *Geophysics* **69**, 1491–1504 (Nov. 2004).

[32] Amundsen, L. and Robertsson, J. O. A., "Wave equation processing using finite-difference propagators, Part 1: Wavefield dissection and imaging of marine multicomponent seismic data," *Geophysics* **79**, T287–T300 (Nov. 2014).

[33] Marty, P., Boehm, C., and Fichtner, A., "Shape optimization for transcranial ultrasound computed tomography," in [*Medical Imaging 2023: Ultrasonic Imaging and Tomography*], **12470**, 77–88, SPIE (Apr. 2023).

[34] Mitcham, T., Ali, R., Schartz, D., Singh, M., Bender, M., and Duric, N., "Feasibility of Imaging Ischemic Stroke Through the Skull Using Ultrasound Tomography," in [*2023 IEEE International Ultrasonics Symposium (IUS)*], 1–3, IEEE, Montreal, QC, Canada (Sept. 2023).

[35] Iacono, M. I., Neufeld, E., Akinnagbe, E., Bower, K., Wolf, J., Vogiatzis Oikonomidis, I., Sharma, D., Lloyd, B., Wilm, B. J., Wyss, M., Pruessmann, K. P., Jakab, A., Makris, N., Cohen, E. D., Kuster, N., Kainz, W., and Angelone, L. M., "MIDA: A Multimodal Imaging-Based Detailed Anatomical Model of the Human Head and Neck," *PLOS ONE* **10**, e0124126 (Apr. 2015).

[36] Coreform LLC, "Coreform Cubit," (2023). Orem, UT: Retrieved from http://coreform.com.

[37] Groos, L., Schäfer, M., Forbriger, T., and Bohlen, T., "The role of attenuation in 2D full-waveform inversion of shallow-seismic body and Rayleigh waves," *Geophysics* **79**, R247–R261 (Nov. 2014).

[38] Pichardo, S., Moreno-Hernández, C., Drainville, R. A., Sin, V., Curiel, L., and Hynynen, K., "A viscoelastic model for the prediction of transcranial ultrasound propagation: application for the estimation of shear acoustic properties in the human skull," *Physics in Medicine & Biology* **62**, 6938–6962 (Aug. 2017).